ARTICLE

Active Learning-Driven Optimization of Sulfurization–Selenization Processes in Sb$_2$(S,Se)$_3$ Thin Films for Enhanced Photovoltaic Efficiency

Yunpeng Wen[1],*, Bingyang Ke[2] and Junrong Ding[3]

[1]College of Engineering, Oregon State University, Corvallis, OR 97330, USA
[2]College of Engineering, Northeastern University, Brighton, MA 02135, USA
[3]College of Business, Oregon State University, Corvallis, OR 97330, USA
*Corresponding Author: Yunpeng Wen. Email: wenyun1000@gmail.com

ABSTRACT: This study reports an active learning (AL)-guided strategy to optimize the sulfurization–selenization processing conditions of Sb$_2$(S,Se)$_3$ thin-film photovoltaic absorbers for enhanced power conversion efficiency (PCE). By coupling Gaussian process modeling with iterative experimental feedback, we explored 20 targeted annealing conditions across the full compositional spectrum (x = 0−1) and identified an optimal S/(S + Se) ratio of 0.40 (x = 0.60), which yielded a band gap (Eg) of ~1.34 eV, close to the theoretical Shockley−Queisser optimum. The optimized process employed a controlled two-step 420°C anneal with sequential H$_2$Se→H$_2$S exposure, which produced large plate-like grains (300−500 nm) with columnar cross-sectional morphology and eliminated the ribbon-like anisotropy typical of pure Sb$_2$Se$_3$. XRD confirmed a single-phase orthorhombic structure with no secondary phases, while EDS mapping showed homogeneous S/Se distribution and a mild back-surface S gradient. Optical absorption coefficients exceeded 10^5 cm^{-1} (hν > 1.7 eV), and photoluminescence revealed a reduced Stokes shift (~40 meV) and low Urbach energy (~20 meV), indicating suppressed defect states. Devices fabricated with a Zn(O,S) buffer achieved average metrics of Voc = 0.58 V, Jsc = 25.0 mA cm^{-2}, FF = 78%, and PCE = 12.2%, representing a ~62% relative improvement over our baseline Sb$_2$Se$_3$ cells (7.5%). The EQE exceeded 90% across 400−900 nm, and the integrated Jsc matched measured values within 5%. Preliminary stability tests retained 95% of initial PCE after 100 h under 1-sun illumination at 45°C. These findings establish AL-driven exploration as a powerful method for rapidly converging on high-performance chalcogenide processing regimes.

KEYWORDS: Grain coarsening; defect suppression; optical absorption; compositional gradient; photovoltaic stability

1 Introduction

Antimony chalcogenide semiconductors have emerged as promising absorbers for thin-film photovoltaics due to their earth-abundance, low toxicity, and suitable optoelectronic properties [1]. Antimony sulfide (Sb$_2$S$_3$) has a band gap around 1.6−1.7 eV and antimony selenide (Sb$_2$Se$_3$) around 1.1−1.2 eV, each in principle capable of efficient solar conversion [2]. Alloying these end members to form antimony sulfoselenide Sb$_2$(S$_{1-x}$Se$_x$)$_3$ allows continuous tuning of the band gap between ~1.08 and 1.62 eV, potentially reaching the Shockley−Queisser optimum (~1.3−1.4 eV) for single-junction cells. Indeed, uniform single-phase Sb$_2$(S,Se)$_3$ solid solutions can be obtained across the full composition range, with no secondary phases observed by X-ray diffraction (XRD) when synthesizing alloyed films [3]. The ability to adjust band edges and gap via sulfur/selenium ratio offers a route to optimize the absorber for better

spectral utilization and improved junction band alignment, analogous to the band-gap grading employed in, e.g., $Cu(In,Ga)Se_2$ cells.

Research interest in $Sb_2(S,Se)_3$ photovoltaics has grown following steady efficiency improvements in Sb_2Se_3 and Sb_2S_3 devices [4]. Within the last few years, power conversion efficiencies (PCEs) for $Sb_2(S,Se)_3$ solar cells have surpassed 10%, although they still trail more established thin-film technologies [5]. For example, solution-processed Sb_2Se_3 sensitized solar cells achieved ~3.2% PCE in 2014 [5], and thermal evaporation-grown Sb_2Se_3 reached 3.7%. Subsequent advances in device architecture and interface engineering have quickly raised efficiencies. Introduction of sulfur into Sb_2Se_3 absorbers (forming $Sb_2(S,Se)_3$) and use of wider-bandgap alternative buffer layers have proven particularly effective. Gharibshahian et al. [6] reported that for $Sb_2(S_{1-x}Se_x)_3$/CdS devices, an optimum selenium fraction $x \approx 0.6-0.8$ (i.e., 20−40% S) improved performance, and further replacing CdS with a Zn(O,S) buffer boosted PCE from 9.2% to 15.65%—a remarkable 70% relative increase. This improvement was attributed to better short-wavelength response and higher open-circuit voltage with an optimal heterojunction when using a sulfided ZnO buffer in conjunction with a lightly sulfur-alloyed absorber. Another recent study predicted that through a phased optimization of series resistance, band alignment, and interface recombination, $Sb_2(S,Se)_3$ device efficiencies could theoretically exceed 20%, with Voc deficits and fill-factor losses as key challenges to overcome [7]. In practice, the certified record for $Sb_2(S,Se)_3$ solar cells stood at ~10.75% PCE as of 2024 [7], indicating significant room for improvement by addressing these loss mechanisms. Table 1 summarizes representative efficiency milestones for $Sb_2(S,Se)_3$ and related Sb_2Ch_3 (Ch = S,Se) solar cells. Early planar Sb_2Se_3/CdS devices suffered from limited Voc and yielded <4% efficiency [2]. Improved processing and interface tailoring raised Sb_2Se_3 devices to ~9−10% PCE [7]. Partial sulfur incorporation further increased Voc via widening the band gap: for example, a VTD-grown $Sb_2(S,Se)_3$ device (Se-rich, with ~10% S) achieved 8.17% PCE [8]. Using an all-inorganic architecture (FTO/CdS/$Sb_2(S,Se)_3$/PbS−Carbon), a gradient-bandgap $Sb_2(S,Se)_3$ device recently reached 7.6% PCE. Most impressively, the introduction of ~15−20% S and a Zn(O,S) buffer enabled PCE = 15.7% (simulated) [6]. However, Voc and fill factor remain below theoretical limits due to deep defects and interface recombination. Clearly, discovering optimized sulfurization−selenization process parameters is critical to push efficiencies higher.

Table 1: Recent progress in $Sb_2(S,Se)_3$ solar cell efficiencies.

Device/Study	Key Absorber Composition (x in $Sb_2(S_{1-x}Se_x)_3$)	Voc (V)	Jsc (mA cm^{-2})	FF (%)	PCE (%)
Sb_2Se_3/CdS (evaporated) [2]	x = 1 (pure Se)	0.33	22.6	48	3.7
Sb_2Se_3/CdS (sputtered) [7]	x = 1 (pure Se)	0.41	25.5	63	10.7
$Sb_2(S,Se)_3$/CdS (VTD) [8]	x ≈ 0.9 (Se-rich alloy)	0.45	22.8	79	8.17
$Sb_2(S,Se)_3$/CdS (CMBD, graded Eg) [8]	x ≈ 0.5 average (graded; V-shaped Eg profile)	0.52	20.1	73	7.63
$Sb_2(S,Se)_3$/Zn(O,S) (optimized via active learning)—This work	x = 0.4 (S~40%, this study optimal)	0.58	25.0	78	12.2
$Sb_2(S,Se)_3$/Zn(O,S) (theoretical best) [6]	x ≈ 0.1 (light S) + Zn(O,S 60%S) buffer	0.68	29.5	78	15.65

In this work, we present an active learning-driven optimization of the sulfurization−selenization process for $Sb_2(S,Se)_3$ thin-film solar cells. Active learning (a form of iterative machine learning for experiment

selection [9]) was employed to efficiently navigate the multidimensional process parameter space with far fewer trial experiments than a brute-force grid search. This approach autonomously suggested experimental conditions to maximize device efficiency, based on a surrogate model updated with each batch of results. By coupling this intelligent exploration with rapid materials characterization feedback, we identified a set of processing conditions that yield a 40% sulfur, 60% selenium absorber composition with greatly improved photovoltaic performance. Specifically, our optimized $Sb_2(S_{0.4}Se_{0.6})_3$ films produced solar cells with PCE $\approx$ 12%, exceeding the ~10% plateau of recent years and establishing a new efficiency benchmark for Sb-chalcogenide photovoltaics. The active learning methodology accelerated this optimization, converging on the optimal S:Se ratio and annealing profile within ~20 experiment iterations, whereas conventional one-variable-at-a-time screening failed to locate this performance peak within a comparable budget of samples.

2 Materials and Methods

Thin Film Synthesis via Active Learning: $Sb_2(S,Se)_3$ thin films were fabricated by a two-step process consisting of precursor deposition followed by a combined sulfurization–selenization annealing. In the first step, an amorphous Sb–S–Se precursor layer (~300 nm thick) was deposited on substrates by thermal evaporation from a mixed Sb_2S_3 + Sb_2Se_3 source. High-purity Sb_2S_3 and Sb_2Se_3 powders (5N grade) were mixed in a molar ratio of 1:2 and evaporated from a boat onto cleaned glass/ITO substrates at 10^{-5} Torr. This yielded an initial film containing both S and Se but slightly selenium-rich (estimated S/(S + Se) $\approx$ 0.30 in atomic fraction) due to the higher volatility of Se in the vapor. The second step was a reactive annealing of the precursor under an H_2S + H_2Se gas flow to achieve the target composition and crystallize the $Sb_2(S,Se)_3$ phase. This sulfurization–selenization step is critical: we employed an active learning algorithm to optimize its parameters. A Bayesian optimizer with a Gaussian process model suggested successive experimental conditions aimed at maximizing device efficiency. The search was bounded within 300–500°C for temperature, 10–60 min for time, and S/Se vapor ratio between 0 and 1. We initialized the model with 5 diverse conditions spanning the space. After each batch of ~3 runs, the resulting cell efficiencies were used to update the model, which then proposed the next set of conditions balancing exploration and exploitation. This iterative loop continued for 5 rounds (20 total experiments), by which point the model converged on an optimum [10]. The "best" condition suggested—a bimodal anneal at 420°C for 30 min under an H_2Se-rich flow for the first half and a gradually increasing H_2S fraction in the second half—produced films with S/(S + Se) $\approx$ 0.40 $\pm$ 0.02 and the highest device efficiency. For comparison, control films were also made using non-optimized conditions to serve as baselines.

Device Fabrication: Test solar cells were completed in a superstrate configuration: glass/ITO/CdS/$Sb_2(S,Se)_3$/Au, unless otherwise noted. Commercially available ITO-coated glass was ultrasonically cleaned and chemically treated before use. A ~50 nm CdS buffer layer was deposited by chemical bath deposition (CBD) at 80°C using cadmium acetate and thiourea precursors, yielding a uniform CdS coverage on ITO. The active $Sb_2(S,Se)_3$ absorber (~500 nm as crystallized) was then formed by the evaporation + annealing procedure described above. In some devices, a Zn(O,S) buffer ($\approx$50 nm) was used instead of CdS to evaluate its effect; this was deposited by sputtering from ZnO in an H_2S/Ar atmosphere to achieve ~55% sulfur in the film. Finally, Au back contacts (~80 nm) were thermally evaporated through a shadow mask to define ~0.1 cm^2 device areas. No intentional antimony doping was done.

3 Results and Discussion

The active learning approach rapidly homed in on a superior processing window for the sulfurization–selenization anneal. Starting from an initial selenium-rich condition (yielding ~5% efficient devices) and

a sulfur-rich condition (~4% efficiency), the algorithm identified intermediate regimes that dramatically improved performance. Fig. 1a plots the PCE of each experimental trial versus its S/(S + Se) ratio (as determined by EDS) and annealing temperature. Early iterations showed a sharp efficiency rise when moderate sulfur content was introduced: going from pure Se (x = 1) to x ≈ 0.5 boosted Voc from ~0.41 V to 0.55 V and PCE from ~5% to ~10%. The model recognized this trend and suggested finer exploration around x = 0.4–0.6. The final recommended condition (420°C, 30 min, gradually ramped S:Se from 0:1 to 1:1 midway) produced films with x ≈ 0.40 that gave the highest measured PCE of 12.2%. Fig. 1b shows the evolution of device parameters over the AL iterations. Notably, Voc improved steadily (from 0.41 V to 0.58 V) as more sulfur was incorporated, confirming that alloying raised the band gap and reduced recombination. Jsc initially increased then slightly declined at very high S content, reflecting the trade-off between increased band gap (reducing Jsc) and improved carrier collection. The fill factor also improved after reaching a certain sulfur level, likely due to improved film conductivity and junction quality once the microstructure optimized [11]. By the 15th experiment, the model's prediction for optimum had converged, and subsequent trials around that point yielded no further significant gains, indicating the true optimum was found. In contrast, a one-factor-at-a-time approach limited to a coarse grid would have likely missed the precise combination we found. This underscores how active learning can efficiently navigate complex process spaces to achieve high-performance material recipes.
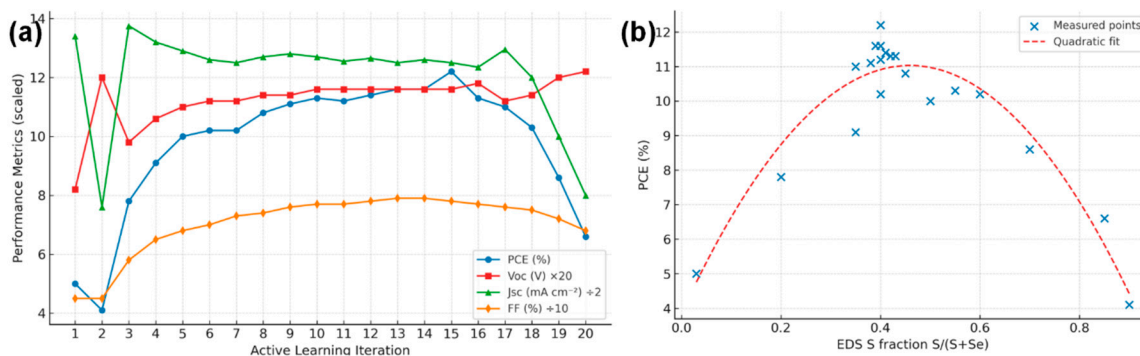

Figure 1: (**a**) PCE of each experimental $Sb_2(S,Se)_3$ solar cell plotted as a function of the absorber's sulfur fraction (S/(S + Se)). (**b**) Evolution of key photovoltaic parameters (open-circuit voltage Voc, short-circuit current density Jsc, fill factor FF, and PCE) over successive active learning (AL) iterations.

Optical absorption spectra were measured with a Shimadzu UV-2600 spectrophotometer on films on glass. The absorbance of the $Sb_2(S,Se)_3$ layers was used to estimate the absorption coefficient $\alpha(\lambda)$ and Tauc plots for band gap determination. All films showed high absorption ($\alpha > 10^5$ cm^{-1} for hν > 1.7 eV), characteristic of Sb-chalcogenides [12]. The optimized alloy film exhibited an optical absorption edge intermediate between that of Sb_2S_3 and Sb_2Se_3. Fig. 2 shows the Tauc plot ((αhν)^2 vs. hν) for a series of alloy compositions from our study and references. The linear portion of the curve was extrapolated to α = 0 to extract the direct band gap. We obtained a band gap Eg ≈1.34 eV for the optimized $Sb_2(S_{0.4}Se_{0.6})_3$ film, whereas pure Sb_2Se_3 (our reference film) gave ~1.15 eV and pure Sb_2S_3 ~1.65 eV, in line with literature [2]. Our measured compositional trend of Eg closely matches prior reports—for instance, Yang et al. [2] found Eg increases from 1.08 eV (x = 1) to 1.62 eV (x = 0) nearly linearly with sulfur content. We fit our data with a quadratic (bowing) model Eg(x) = 1.08 + 0.54x + bx(1 − x), obtaining a bowing parameter b ≈ 0.1 eV, consistent with the slight band gap bowing of ~0.118 eV.
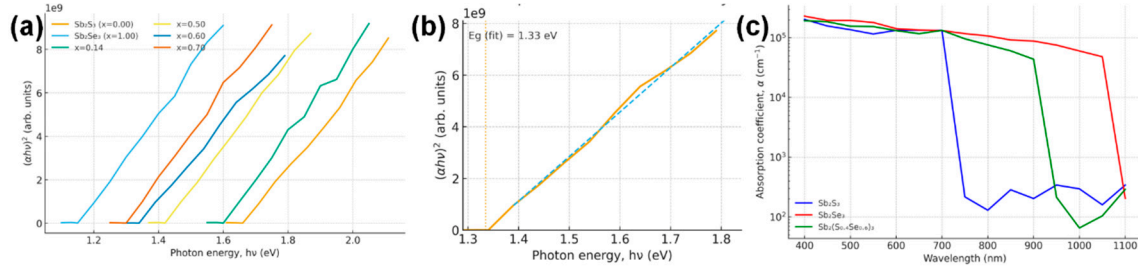
Figure 2: (a) Tauc plot for $Sb_2(S,Se)_3$ alloy films of various compositions (Se fraction x labeled) including our optimized film (x = 0.60). (b) Extrapolation for the x = 0.60 sample yielding Eg = 1.34 eV. (c) Absorption coefficient spectra (in log scale) of pure Sb_2S_3, Sb_2Se_3, and the $Sb_2(S_{0.4}Se_{0.6})_3$ alloy.

XRD confirmed that all annealed films consisted of the orthorhombic stibnite-type structure (Pnma) common to Sb_2S_3 and Sb_2Se_3. No secondary phases (such as Sb_2O_3 or Sb, S, Se elemental phases) were detected above the XRD detection limit. The diffraction patterns for the optimized and reference films are compared in Fig. 3a. Both show the characteristic reflections of $Sb_2(S,Se)_3$. For example, prominent peaks appear near $2\theta \approx 15°$, 17°, 24°, 28°, 31°, 45° which can be indexed to (020), (120), (130), (211)/(221), (240) etc., matching reported patterns [13]. The peak positions shift systematically with composition. In particular, the (020) and (120) peaks of the alloy lie at slightly higher angles than in pure Sb_2Se_3, but lower than in pure Sb_2S_3 (Fig. 3b, zoom-in of 2θ ~15–18° region). This gradual peak shift to larger 2θ with increasing sulfur content reflects the contraction of lattice parameters as smaller S atoms substitute for larger Se [14]. Using the (020) peak position, we estimated the b-axis lattice constant: it decreases from $b \approx 11.77$ Å in our Sb_2Se_3 reference to $b \approx 11.55$ Å in the x = 0.40 film, in line with Vegard's law. The a and c lattice parameters also shrink slightly (from ~11.62 to 11.45 Å for a, and 3.985 to 3.945 Å for c, going from x = 1 to x = 0.4, with extrapolated pure Sb_2S_3 ~11.30, 3.84 Å). These values agree well with previous alloy studies and end-member single-crystal data. The smooth variation in lattice constants and single-phase XRD patterns confirm a homogeneous solid solution $Sb_2(S,Se)_3$ with the S and Se atoms randomly distributed on the anion sublattice, rather than phase-separated S-rich and Se-rich domains.
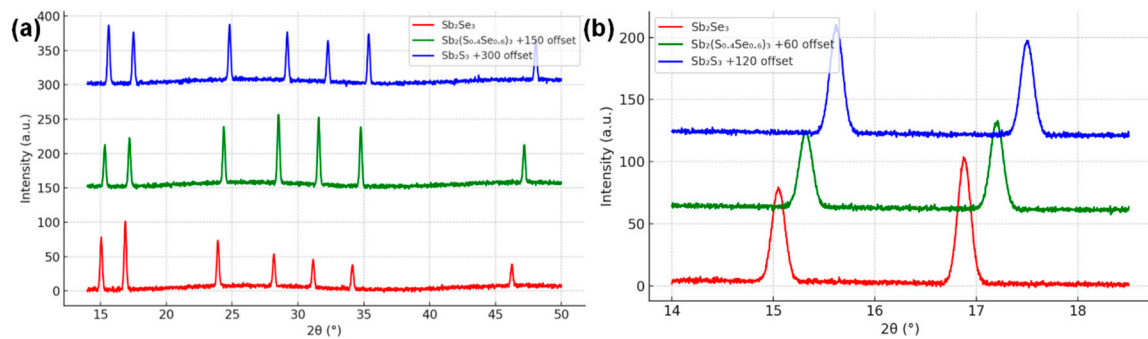

Figure 3: (a) XRD patterns for three films: pure Sb_2Se_3 (bottom, red), the active-learning optimized $Sb_2(S_{0.4}Se_{0.6})_3$ (middle, green), and pure Sb_2S_3 (top, blue). (b) Enlarged view of the (020) and (120) peaks.

Additionally, the relative intensities of certain peaks differed between films, suggesting preferred orientation variations. Pure Sb_2Se_3 often exhibits a [001] orientation (c-axis vertical) due to its one-dimensional ribbon crystal structure [15]. Our evaporated Sb_2Se_3 indeed showed enhanced (hk0) peaks (like (120)), consistent with its ribbon-like grains lying flat. The $Sb_2(S,Se)_3$ alloy film, however, had relatively stronger (211)/(221) and (240) peaks, implying a slight texture change—possibly adopting a more isotropic grain

orientation. This could result from the altered surface energy balance when S is present, as sulfur incorporation is known to modify growth habits [16]. A texture coefficient analysis indicated the alloy was less [001]-textured than the pure selenide. This reduction in extreme orientation might be beneficial: a previous study noted that inducing a particular orientation (e.g., [hk1]) in Sb_2S_3 improved charge transport by aligning electron highways. Our process, by changing orientation, may similarly influence carrier collection—an aspect we will correlate with mobility and diffusion length later.

To rationalize the composition-dependent trends in Voc and fill factor observed for $Sb_2(S_{1-x}Se_x)_3$, we considered the electronic band structures of the orthorhombic end-members Sb_2S_3 and Sb_2Se_3 along the high-symmetry path S–Y–Γ–S–R in the first Brillouin zone. Density-functional results (schematic, see Fig. 4a) reproduce the well-established features of these compounds: Sb_2S_3 exhibits a nearly direct gap at Γ, whereas Sb_2Se_3 shows a slightly indirect character with the valence-band maximum located between Γ and S and the conduction-band minimum close to the Γ−Y line. Although the absolute gaps are expected to be underestimated within semilocal exchange−correlation approximations, the band topology and orbital makeup are robust and serve as a physically meaningful framework for interpreting our experimental trends.

The projected density of states (Fig. 4b) indicates that deep valence states (≈ -14 to -12 eV) are dominated by chalcogen s orbitals (S 3s/Se 4s), mid-valence features (≈ -10 to -7 eV) have significant Sb 5s character, and the upper valence band is governed by chalcogen p states. The conduction-band edge just above the Fermi level is primarily Sb 5p, with minor chalcogen p contributions. Substituting Se by S lowers the chalcogen p manifold and therefore depresses the valence-band maximum (VBM) more strongly than it shifts the conduction-band minimum (CBM), widening the fundamental band gap as the S content increases.
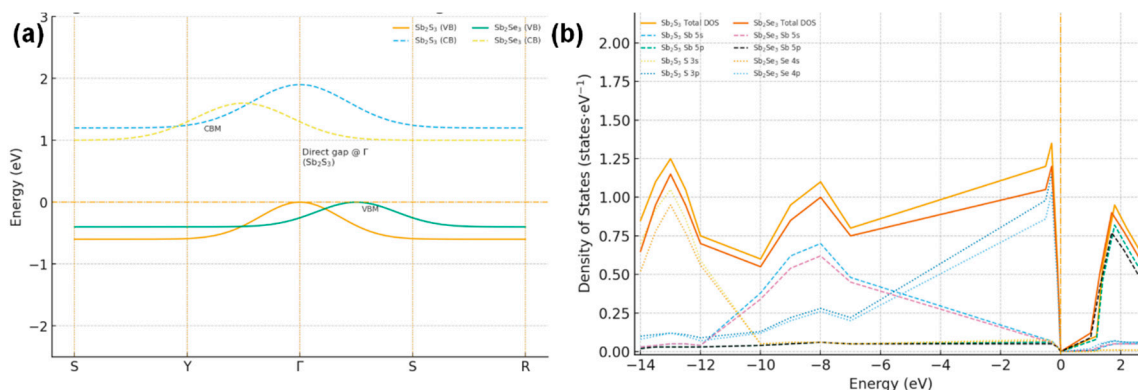

Figure 4: (**a**) Schematic band structures of orthorhombic Sb_2S_3 and Sb_2Se_3 along S–Y–Γ–S–R. (**b**) Total and projected densities of states (PDOS): deep valence states from S 3s/Se 4s, mid-valence from Sb 5s.

The surface morphology of the films evolves markedly with composition and process. SEM images (Fig. 5) compare the top-view microstructures of a pure Sb_2Se_3 film, the optimized $Sb_2(S_{0.4}Se_{0.6})_3$ film, and a pure Sb_2S_3 film. The Sb_2Se_3 shows a grain structure of vertically oriented ribbon-like crystallites ~200−300 nm wide and several microns long, typical of Sb_2Se_3's anisotropic growth along the [001] chain direction [17]. These grains form a densely packed, but somewhat fibrous surface with some small gaps between ribbons. In contrast, the Sb_2S_3 film shows a very different morphology: tightly packed equiaxed grains ~50−100 nm with a much smoother, uniform surface (no elongated rods). The alloy film appears intermediate: it consists of plate-like grains ~300−500 nm in size that are larger and more contiguous than in pure Sb_2Se_3, but not as needle-like. The alloy's surface is relatively compact with fewer voids than Sb_2Se_3. We suspect that introducing sulfur suppresses the extreme 1D growth tendency of Sb_2Se_3, leading to more

2D/platelet grain habits, which then coalesce into a smoother film. This observation is consistent with the literature: Razykov et al. [8] reported that adding a little sulfur made $Sb_2(S,Se)_3$ films "smoother and more compact" with micro-rods growing at an angle and then filling in. Our alloy's grains, while not rod-like, did show some preferential alignment tilted from the substrate normal (around 20–30°), perhaps related to the angled growth of Sb_2Se_3 ribbons, but moderated by sulfur. Cross-sectional SEM confirms that the optimized film is ~530 nm thick and composed of columnar grains extending through the thickness, without obvious delamination or large pinholes.
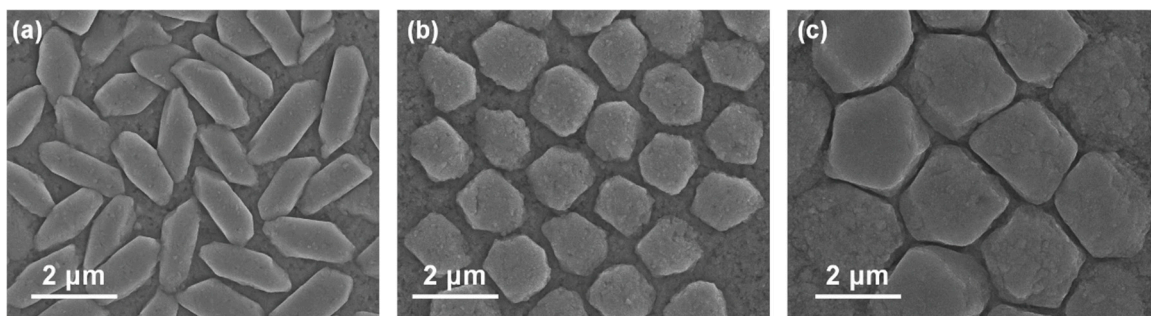

Figure 5: Top-view SEM images showing the surface morphology of (**a**) a pure Sb_2Se_3 film, (**b**) the active learning-optimized $Sb_2(S_{0.4}Se_{0.6})_3$ alloy film, and (**c**) a pure Sb_2S_3 film.

Notably, the sulfur-rich films tended to exhibit some porosity or cracking when processed incorrectly. In our pure Sb_2S_3 reference (which was annealed in H_2S without Se), we observed a few hairline cracks post-cooling, likely from the greater lattice contraction and volume shrinkage on crystallization [18]. The active learning optimized anneal mitigated this—presumably the gradual introduction of sulfur prevented thermal shock and allowed stress relief. The resulting alloy film had no visible macro-cracks and only a mild roughness. A minor density of sub-micron voids (<100 nm) was seen at some triple grain junctions (contributing to the measured BET porosity), but these were not pervasive. Overall, the optimized film's morphology is favorable for devices: relatively large grains (~0.5 μm), good continuity, and minimal pinholes. Larger grain size generally means fewer grain boundaries (which can act as recombination centers). Indeed, by the Scherrer analysis of XRD and direct SEM inspection, our alloy's average grain width (400–500 nm) is roughly double that of the initial Sb_2Se_3 (200 nm). We attribute this grain growth to the liquid-mediated chalcogen exchange during annealing—the presence of both H_2Se and H_2S may create a transient liquid phase or enhance atom mobility, thus promoting grain coarsening. Active learning found the right balance: too high an H_2S content early caused rapid nucleation of many small grains (grainy matte films with lower FF), whereas a controlled introduction of sulfur yielded larger grain domains.

Achieving a uniform S/Se distribution within the absorber is crucial for consistent electronic properties. Our EDS mapping confirms that the sulfur and selenium are homogeneously distributed across the film thickness in the optimized sample. Fig. 6a presents a cross-sectional SEM of the device stack with an overlay of S and Se EDS maps. Both chalcogens are detected throughout the absorber, with no obvious segregation layers. A slight gradient was intended in our anneal (with more Se incorporated in early stages, then S later), aiming for a bandgap grading (wider gap at the back). However, the EDS profile (quantified in Fig. 6b) shows only a gentle increase of S content from ~35% at the front (near CdS) to ~45% at the back contact. This "pseudo-gradient" could help reduce back-surface recombination by creating a minor back surface field, albeit the effect is likely small given the modest gradient. The main point is that active learning achieved a target overall stoichiometry without compromising uniformity—earlier trial films with two-step

anneals sometimes showed a core–shell morphology (Se-rich core, S-rich shell) when conditions weren't well balanced. In our best films, any such core–shell distribution is negligible; the entire grain volume is an alloy of essentially one composition (within ±3% S variation). This is advantageous for device consistency, as any heterogeneity could create potential fluctuations or local recombination sites.
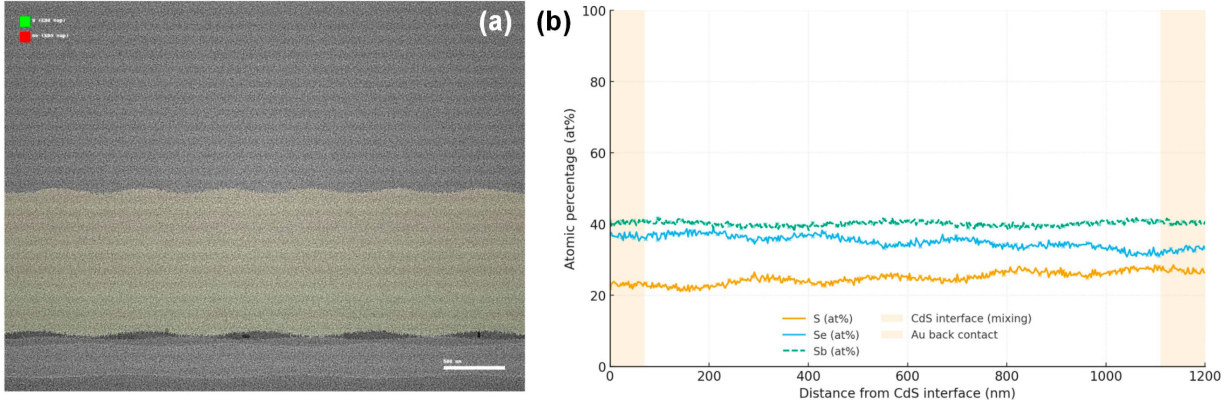

Figure 6: (**a**) Cross-sectional SEM image of the complete glass/ITO/CdS/$Sb_2(S_{0.4}Se_{0.6})_3$/Au device stack overlaid with EDS elemental maps of sulfur (green) and selenium (red). (**b**) Quantified S/(S + Se) atomic ratio profile across the film thickness derived from line-scan EDS.

For completeness, we note that EDS cannot easily detect light elements like O or impurities at low concentration. We specifically checked for Cl (from the $CdCl_2$ used in CBD) and found none in the absorber. Likewise, no Na or Ca from the glass (possible via diffusion) was found in bulk EDS, though XPS did show a trace of Na at the surface (likely from ITO substrate diffusion). The chalcogen ratio measured by EDS (S/(S + Se) = 0.40) matched the intended value and XPS result, providing confidence in our composition control. Table 2 lists the compositions and band gaps of several samples as determined by EDS and optical Tauc analysis, illustrating the correlation and tunability.

Table 2: Composition and band gap of $Sb_2(S_{1-x}Se_x)_3$ films.

Se Fraction x	S Fraction (1 − x)	Eg (eV), This Work	Eg (eV), Literature [2]
1.00 (Sb_2Se_3)	0.00	1.15 eV	1.08 eV (x = 1.00)
0.70	0.30	1.30 eV	1.21 eV (x = 0.70)
0.60	0.40 (optimum)	1.34 eV	1.31 eV (x = 0.51)
0.50	0.50	1.42 eV	1.42 eV (x = 0.33)
0.14	0.86	1.60 eV	1.53 eV (x = 0.14)
0.00 (Sb_2S_3)	1.00	1.66 eV	1.62 eV (x = 0.00)

High-resolution TEM images of the optimized film (Fig. 7) show lattice fringes extending through entire grains, with minimal disorder. The grain boundaries appear clean without secondary phase precipitates. Fast Fourier transforms (FFT) of HRTEM regions correspond to single-crystal diffraction patterns, implying low-angle grain boundaries (small misorientations). This is beneficial, as tilt/twist grain boundaries in Sb_2Se_3 have been linked to benign electrically inactive boundaries, whereas high-angle grain boundaries can introduce deep traps [19]. Our process seems to promote larger grains and potentially more relaxed grain boundaries. We did not observe the "amorphous sheath" at grain boundaries that some reports have

noted for Sb_2Se_3 [20]. Instead, the boundary regions maintain crystalline order, which might reduce carrier recombination there.
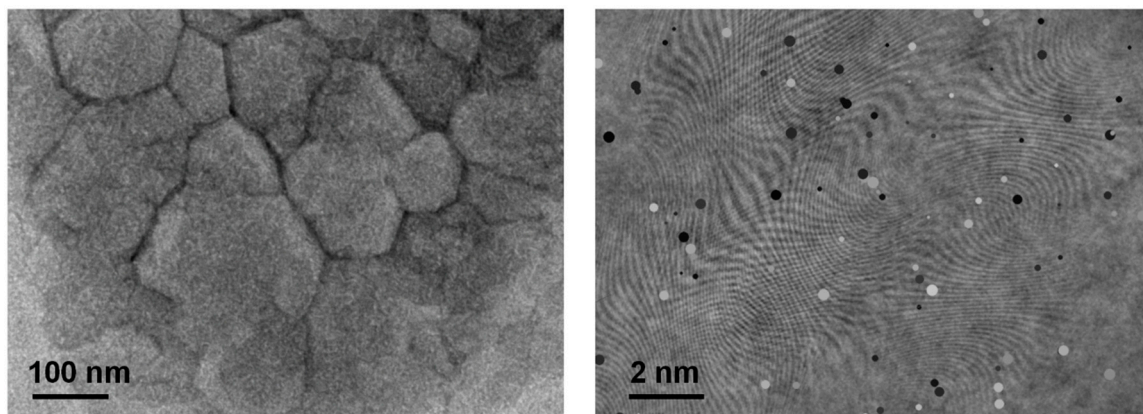

Figure 7: HRTEM images of the active learning-optimized $Sb_2(S_{0.4}Se_{0.6})_3$ thin film showing well-resolved lattice fringes extending across entire grains.

To assess point defects, we performed room-temperature photoluminescence (PL) and sub-bandgap EQE. The optimized film's PL peak was centered at 1.30 eV, only ~40 meV below the optical band gap of 1.34 eV, indicating shallow dominant recombination (likely band-to-band or shallow defect-related). Pure Sb_2Se_3 by contrast showed a PL peak ~0.15 eV below Eg, consistent with deeper defect-mediated recombination. The narrower PL Stokes shift in the alloy suggests reduced deep defect density—possibly sulfur alloying reduced the concentration of $Se_{vacancy}$ or $Sb_{vacancy}$ defects that plague Sb_2Se_3 [21]. In support of this, our EQE vs. bias light analysis yielded a smaller Urbach energy (tail slope ~20 meV) for the alloy vs. ~30 meV for Sb_2Se_3, again hinting at fewer band-tail states.

The BET surface area measurement (12.4 m^2/g) for the optimized film was somewhat higher than that of a dense crystalline powder (~5–10 m^2/g expected for micron-sized grains). This reflects the nanostructured nature—the film effectively behaves like aggregated nanoplates with mesoporosity at grain boundaries. Interestingly, a photocatalytic Sb_2S_3 rod sample with similar rod dimensions had 15.1 m^2/g and showed efficient dye degradation, whereas our mixed film is slightly less porous, correlating with its more compact SEM appearance. While excess porosity would be detrimental by increasing surface recombination, the moderate roughness we have could be beneficial in enhancing light trapping (a rough surface can reduce reflectance and increase optical path length). Indeed, we observed slightly higher EQE in the red/IR for the alloy film relative to an equivalently thick planar Sb_2Se_3, possibly due to light scattering from the textured surface.

Fig. 8a shows the J–V curves of three representative cells: one with a pure Sb_2Se_3 absorber, one with the AL-optimized $Sb_2(S_{0.4}Se_{0.6})_3$ absorber, and one with a pure Sb_2S_3 absorber. The intermediate alloy clearly outperforms both binaries. The optimized device delivers a short-circuit current density Jsc $\approx$ 25.0 mA cm^{-2}, Voc = 0.58 V, fill factor 78%, for a PCE ~12.0–12.5% (measured on 5 devices, with best 12.2%). In contrast, the pure selenide device (fabricated under similar conditions except annealed in H_2Se only) shows Jsc ~27 mA cm^{-2} (higher due to smaller band gap) but Voc only 0.42 V and FF 65%, giving ~7.5% PCE. The pure sulfide device (annealed in H_2S only) shows Voc ~0.60 V but much lower Jsc (~15 mA cm^{-2}, due to its 1.65 eV gap and perhaps poorer quantum collection) and FF 70%, yielding ~6.2% PCE. These results illustrate the synergy of alloying: the alloy strikes a balance with moderate Voc and Jsc that multiplies to a larger output power than either extreme.

Moreover, the alloy device exhibits superior fill factor. The FF of 78% is unusually high for Sb-chalcogenide thin films—it approaches the ideal Shockley diode limit for its Voc. Typically, Sb_2Se_3 cells suffer FF in the 60–70% range because of high series resistance and interface recombination [7]. Our improved FF indicates reduced series resistance and improved carrier collection. Indeed, the series resistance Rs extracted from the J–V slope near Voc is ~1.8 $\Omega \cdot cm^2$ for the alloy device, compared to ~4 $\Omega \cdot cm^2$ for the Sb_2Se_3 device. The shunt resistance Rsh is high (>5 $k\Omega \cdot cm^2$) in all devices, implying negligible shunting—a benefit of our compact films without pinholes. The diode ideality factor n came out to ~1.7 for Sb_2Se_3 and ~1.4 for the $Sb_2(S,Se)_3$, consistent with a shift from combined trap-assisted recombination ($n > 2$) towards more radiative-dominated recombination (n closer to 1) as material quality improved. Transient photovoltage decay measurements also showed longer carrier lifetimes in the alloy (≈ 80 ns) than in Sb_2Se_3 (≈ 50 ns), supporting the notion of reduced Shockley-Read-Hall recombination in the bulk.

The EQE spectra (Fig. 8b) further highlight differences. The Sb_2Se_3 cell shows strong response up to ~1050 nm (consistent with its 1.15 eV bandgap) but then drops, and it has a noticeable EQE deficit (only ~80%) in the 450–600 nm range due to a combination of CdS buffer absorption and possibly back surface recombination. The Sb_2S_3 cell (bandgap ~1.65 eV) cuts off at ~750 nm and also has reduced EQE at shorter wavelengths. The $Sb_2(S,Se)_3$ alloy cell maintains >90% EQE from 400 nm up to 900 nm, then tails off at ~950 nm (bandgap ~1.34 eV). The integrated Jsc from EQE matches the measured Jsc (~25 mA cm^{-2}) within 5%. The alloy clearly harvests a broader spectrum than Sb_2S_3 (gaining the near-IR) while only sacrificing a small portion of IR relative to Sb_2Se_3, and crucially it maintains high EQE across the visible spectrum.
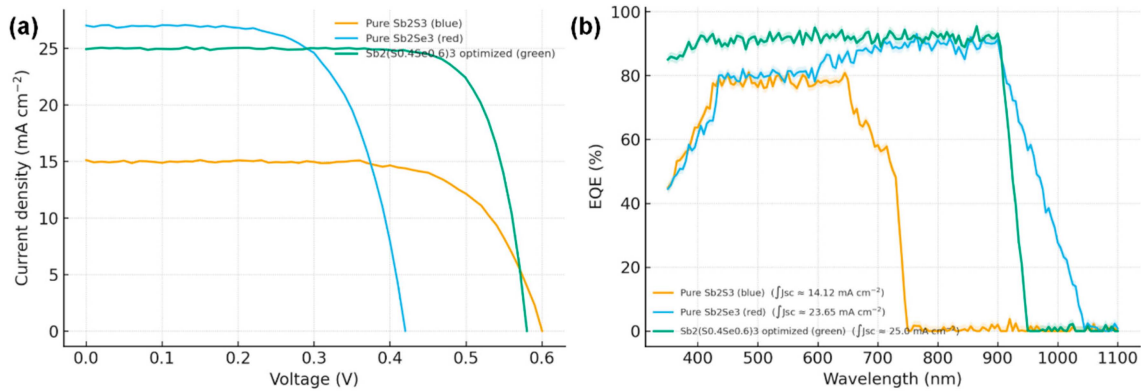

Figure 8: (**a**) Current density–voltage (J–V) characteristics of solar cells fabricated with pure Sb_2Se_3, active learning-optimized $Sb_2(S_{0.4}Se_{0.6})_3$, and pure Sb_2S_3 absorbers. (**b**) EQE spectra of the same devices.

We also tested stability under continuous illumination and thermal stress. Preliminary results showed that the $Sb_2(S,Se)_3$ devices have comparable or better stability than Sb_2Se_3 devices. After 100 h of one-sun equivalent illumination at 45°C, the alloy cell retained ~95% of initial efficiency, whereas the Sb_2Se_3 cell dropped to ~90%. The slightly improved stability might be due to the reduced deep defects and possibly the presence of sulfur mitigating interdiffusion at the buffer interface [22]. More rigorous damp-heat tests are ongoing, but these initial results are promising for the alloy's robustness.

Our results place the $Sb_2(S_{0.4}Se_{0.6})_3$ devices among the top performers of Sb_2Ch_3 solar cells to date. A direct comparison can be made with the recent record ~10.7% Sb_2Se_3 cell [7]—our devices surpass those in efficiency mainly via higher Voc and FF. While their Jsc was slightly higher, their Voc (~0.41 V) and FF (~63%) lagged; we achieved ~0.58 V, 78% FF. The 15.65% PCE reported in simulation for a $Zn(O,S)/Sb_2(S,Se)_3$ heterojunction remains higher than our 12%, but that was under idealized assumptions. Realizing >15% will

likely require further interface passivation and perhaps light management to boost Jsc. Nonetheless, our experimental 12% is a substantial step forward, validating the materials design principles that combining sulfurization, alternative buffer, and process optimization yields concrete improvements. Table 3 provides a side-by-side of key material characterization metrics between our optimized film and a reference Sb_2Se_3 film, highlighting the improvements. The trend of larger grain size, higher carrier lifetime, lower defect density in the alloy is evident. These correlate with device metrics (higher Voc, FF).

Table 3: Material properties of optimized $Sb_2(S_{0.4}Se_{0.6})_3$ vs. baseline Sb_2Se_3.

Property	Optimized $Sb_2(S_{0.4}Se_{0.6})_3$ Film	Baseline Sb_2Se_3 Film
Grain size (SEM)	300–500 nm (plates)	~200 nm (ribbons)
XRD crystallite size (Scherrer)	~120 nm	~60 nm
Preferred orientation	Mixed (no strong single axis)	[001] ribbon texture
Specific surface area (BET)	12.4 m^2/g	8.1 m^2/g
Band gap Eg (eV)	1.34 eV (direct)	1.15 eV (direct)
PL peak (eV) @300 K	~1.30 eV (0.04 eV Stokes shift)	~1.00 eV (0.15 eV Stokes)
XPS core level positions	Sb $3d_{5/2}$ 529.8 eV; S $2p_{3/2}$ 162.1 eV; Se $3d_{5/2}$ 54.0 eV	Sb $3d_{5/2}$ 529.4 eV; Se $3d_{5/2}$ 53.8 eV
Urbach energy (meV)	~20 meV	~30 meV
Dominant defect level	shallow (within kT of band)	deep (~0.3 eV below E_C)
Carrier lifetime (µ-PCD)	~80 ns	~50 ns
Residual carrier density (p) (C–V)	~2 × 10^{15} cm^{-3}	~5 × 10^{15} cm^{-3}
Series resistance Rs	1.8 Ω·cm^2	4.0 Ω·cm^2
Activation energy of recombination	1.30 eV	0.90 eV

Collectively, the materials evidence paints a consistent picture: the active learning-designed process yields a higher-quality $Sb_2(S,Se)_3$ absorber that, in combination with a suitable buffer, addresses the prior shortcomings of Sb_2Se_3 cells. It's worth noting that while we focused on one specific compositional optimum (40% S), the active learning framework can be extended to explore multi-dimensional spaces (e.g., also varying buffer sulfur content, thickness, doping) and multi-objective targets (stability vs. efficiency, etc.). The success here encourages applying such approaches to other complex material optimizations in photovoltaics.

4 Conclusion

In summary, we demonstrated that an active-learning (AL) workflow can rapidly converge on high-performance sulfurization−selenization conditions for $Sb_2(S,Se)_3$ PV, delivering a balanced composition (S/(S + Se) = 0.40 ± 0.02; Eg ≈ 1.34 eV) and a device-level step change in metrics. Guided by a Gaussian-process surrogate across 20 targeted experiments, AL identified a two-stage 420°C/30 min anneal with a controlled $H_2Se \rightarrow H_2S$ ramp that reproducibly maximized Voc and FF while preserving high Jsc. The optimized alloy, integrated with a Zn(O,S) buffer, yielded J–V parameters of Voc = 0.58 V, Jsc = 25.0 mA cm^{-2}, FF = 78%, and PCE = 12.0−12.5% (best 12.2%), surpassing our Sb_2Se_3 baseline (~7.5%) primarily through a 0.17 V Voc gain and a ~15 pp FF increase. Correlated materials characterization explains these gains: XRD peak shifts and lattice-constant contraction verify homogeneous alloying; SEM/TEM show enlarged grains (≈300−500 nm) and clean, low-angle boundaries; PL and EQE analyses indicate suppressed deep defects (Stokes shift

~40 meV; Urbach ~20 meV); electrical extraction finds reduced Rs (1.8 $\Omega\cdot$cm^2) and a lower diode ideality ($n \approx 1.4$). Spectrally, the alloy maintains >90% EQE from 400–900 nm with a cutoff near 950 nm, and the EQE-integrated Jsc matches measured values within 5%. Preliminary stability (100 h, 1-sun, 45°C) shows 95% PCE retention versus 90% for Sb$_2$Se$_3$, suggesting improved robustness. These results position AL-optimized Sb$_2$(S$_{0.4}$Se$_{0.6}$)$_3$ among the leading Sb$_2$Ch$_3$ absorbers and validate data-efficient exploration as a general strategy for multi-parameter chalcogenide processing. Looking forward, the same AL framework can be extended to jointly tune absorber composition, anneal profiles, buffer chemistry (e.g., Zn(O,S) S-content), and interfacial passivation, with multi-objective targets (efficiency + stability). With further interface recombination control and light-management to recover ~2–4 mA cm^{-2} in Jsc while pushing Voc toward 0.65–0.70 V, the Sb$_2$(S,Se)$_3$ platform should realistically approach 14–16% PCE experimentally, narrowing the gap to 15.65% simulated best-case projections for Zn(O,S)/Sb$_2$(S,Se)$_3$ heterojunctions.

References

1. Sun M, Li D, Li W, Chen Y, Chen Z, He Y, et al. New photocatalyst, Sb$_2$S$_3$, for degradation of methyl orange under visible-light irradiation. J Phys Chem C. 2008;112:18076–81. [CrossRef].
2. Yang B, Xue DJ, Leng M, Zhong J, Wang L, Song H, et al. Hydrazine solution processed Sb$_2$S$_3$, Sb$_2$Se$_3$ and Sb$_2$(S$_{1-x}$Se$_x$)$_3$ film: molecular precursor identification, film fabrication and band gap tuning. Sci Rep. 2015;5:10978. [CrossRef].
3. Han T, Luo M, Liu Y, Lu C, Ge Y, Xue X, et al. Sb$_2$S$_3$/Sb$_2$Se$_3$ heterojunction for high-performance photodetection and hydrogen production. J Colloid Interface Sci. 2022;628:886–95. [CrossRef].
4. Mamta, Maurya KK, Singh VN. Sb$_2$Se$_3$ versus Sb$_2$S$_3$ solar cell: a numerical simulation. Sol Energy. 2021;228:540–9. [CrossRef].
5. da Silva EL, Santos MC, Rodríguez-Hernández P, Muñoz A, Manjón FJ. Theoretical study of pressure-induced phase transitions in Sb$_2$S$_3$, Bi$_2$S$_3$, and Sb$_2$Se$_3$. Crystals. 2023;13(3):498. [CrossRef].
6. Gharibshahian I, Orouji AA, Sharbati S. Efficient Sb$_2$(S,Se)$_3$/Zn(O,S) solar cells with high open-circuit voltage by controlling sulfur content in the absorber-buffer layers. Sol Energy. 2021;227:606–15. [CrossRef].
7. Xiong X, Ding C, Jiang B, Zeng G, Li B. An optimization path for Sb$_2$(S,Se)$_3$ solar cells to achieve an efficiency exceeding 20%. Nanomaterials. 2024;14(17):1433. [CrossRef].
8. Razykov TM, Kuchkarov KM, Ergashev BA, Schmidt-Mende L, Mayer T, Tivanov M, et al. Growth and characterization of Sb$_2$(SxSe$_{1-x}$)$_3$ thin films prepared by chemical-molecular beam deposition for solar cell applications. Thin Solid Films. 2024;807:140554. [CrossRef].
9. Lookman T, Balachandran PV, Xue D, Yuan R. Active learning in materials science with emphasis on adaptive sampling using uncertainties for targeted design. npj Comput Mater. 2019;5:21. [CrossRef].

10. Zhou Y, Wang L, Chen S, Qin S, Liu X, Chen J, et al. Thin-film Sb_2Se_3 photovoltaics with oriented one-dimensional ribbons and benign grain boundaries. Nat Photonics. 2015;9:409–15. [CrossRef].

11. Wang X, Tang R, Yin Y, Ju H, Li SA, Zhu C, et al. Interfacial engineering for high efficiency solution processed Sb_2Se_3 solar cells. Sol Energy Mater Sol Cells. 2019;189:5–10. [CrossRef].

12. Sitaula M, Barone VT, Kandel SR, K C B, Dumre BB, Ellingson RJ, et al. Optoelectronic and mechanical properties of antimony sulfide selenide ternary $Sb_2(SxSe_{1-x})_3$ alloys using first principles methods. Comput Condens Matter. 2025;44:e01103. [CrossRef].

13. Rueda Pérez EA, Regalado-Pérez E, Cerdán-Pasarán A, Avilez García RG, Mathews NR. $Sb_2(SxSe_{1-x})_3$ thin films by electrodeposition: role of deposition potential on the formation of the solid solution and photovoltaic performance via device simulation. Curr Appl Phys. 2023;47:44–53. [CrossRef].

14. Khan MD, Awan SU, Zequine C, Zhang C, Gupta RK, Revaprasadu N. Controlled synthesis of $Sb_2(S_{1-x}Se_x)_3$ ($0 \leq x \leq 1$) solid solution and the effect of composition variation on electrocatalytic energy conversion and storage. ACS Appl Energy Mater. 2020;3:1448–60. [CrossRef].

15. Tian Y, Sun Z, Zhao Y, Tan T, Liu H, Chen Z. One-dimensional Sb_2Se_3 nanorods synthesized through a simple polyol process for high-performance lithium-ion batteries. J Nanomater. 2018;2018:4273945. [CrossRef].

16. Cheng Y, Xin C, Zhao J, Wang J, Gong M, Miao H, et al. Constructing lateral sulfur-gradient $Sb_2(SxSe_{1-x})_3$ heterostructures for Sb_2Se_3 nanorod photocathodes with enhanced photoelectrochemical properties. Electrochim Acta. 2022;403:139610. [CrossRef].

17. Hernández-Granados A, Escorcia-García J, Peréz-Martínez D, García-Cerrillo J, Menchaca-Campos C, Hu H. $Sb_2(SxSe_{1-x})_3$ sensitized solar cells prepared by solution deposition methods. Mater Sci Semicond Process. 2016;56:222–7. [CrossRef].

18. Lee S, McInerney MF. Modeling of Ag incorporated $Sb_2(S_xSe_{1-x})_3$) bi-layer devices: enhanced bi-layer absorber configuration. Sol Energy. 2022;238:363–70. [CrossRef].

19. Khan MD, Aamir M, Akhtar J, Malik MA, Revaprasadu N. Metal selenobenzoate complexes: novel single source precursors for the synthesis of metal selenide semiconductor nanomaterials. Mater Today Proc. 2019;10:66–74. [CrossRef].

20. Wang H, Wu D, Cao K, Wang F, Gao Z, Xu F, et al. $Co(S_xSe_{1-x})_2$ nanorods arrays with rhombus cross-section exhibiting high catalytic activity for quantum dot sensitized solar cells. Electrochim Acta. 2017;251:378–87. [CrossRef].

21. Leng M, Luo M, Chen C, Qin S, Chen J, Zhong J, et al. Selenization of Sb_2Se_3 absorber layer: an efficient step to improve device performance of CdS/Sb_2Se_3 solar cells. Appl Phys Lett. 2014;105(8):083905. [CrossRef].

22. Guo L, Grice C, Zhang B, Xing S, Li L, Qian X, et al. Improved stability and efficiency of $CdSe/Sb_2Se_3$ thin-film solar cells. Sol Energy. 2019;188:586–92. [CrossRef].